Supplementary Material: Modeling Complex Polycrystalline Alloys Using a Generative Adversarial Network (GAN)-Enabled Computational Platform

Brayan Murgas[1], Joshua Stickel[1], Luke Brewer [2], Somnath Ghosh [1]

[1] Department of Civil & Systems Engineering, Johns Hopkins University, Baltimore, MD 21218

[2] Professor, Department of Materials Science & Engineering, University of Alabama, Tuscaloosa, Al

Corresponding author: sghosh20@jhu.edu; Tel: +1-410-516-7833; fax: +1-410-516-7473

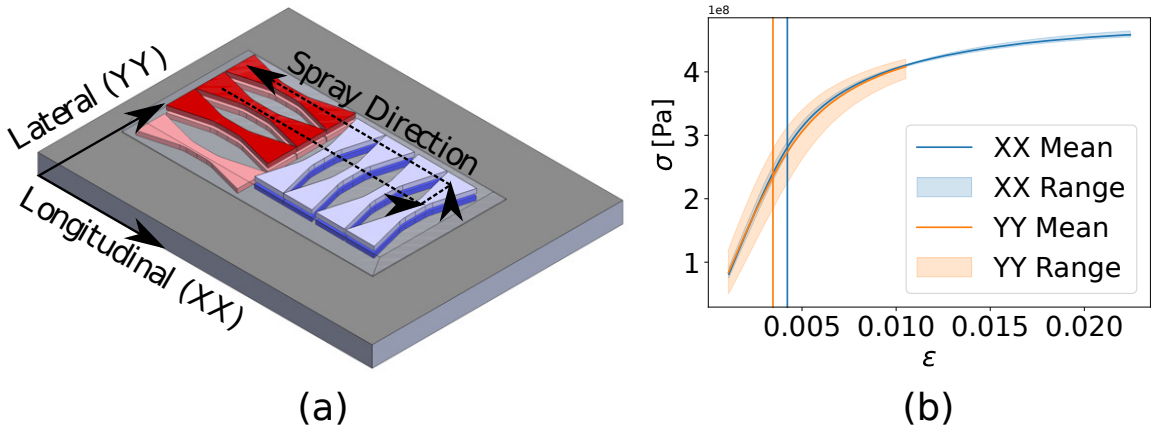
I. Material and processing parameters and mechanical testing data

Elem. Wgt%	Al	Zr	Si	Fe	Cu	Mn	Mg	Cr	Zn	Ti	Other
Min	87.3	0.08	-	-	2.0	-	1.9	-	5.7	-	-
Max	90.3	0.15	0.12	0.15	2.6	0.1	2.6	0.04	6.7	0.06	0.15

Supplementary Table 1: Chemical composition of the CSF AA7050 alloy (weight percent)

Carrier Gas	Pressure	Temperature	Powder Feed Velocity	Gun velocity
Helium	3.45 MPa	450 °C	8.2 g min^{-1}	200 mm s^{-1}
Stand-off Distance	Nozzle Length	Nozzle Throat Diameter	Nozzle Exit Diameter	
15 mm	150 mm	2 mm	4 mm	-

Supplementary Table 2: Information of the cold spray forming process parameters.

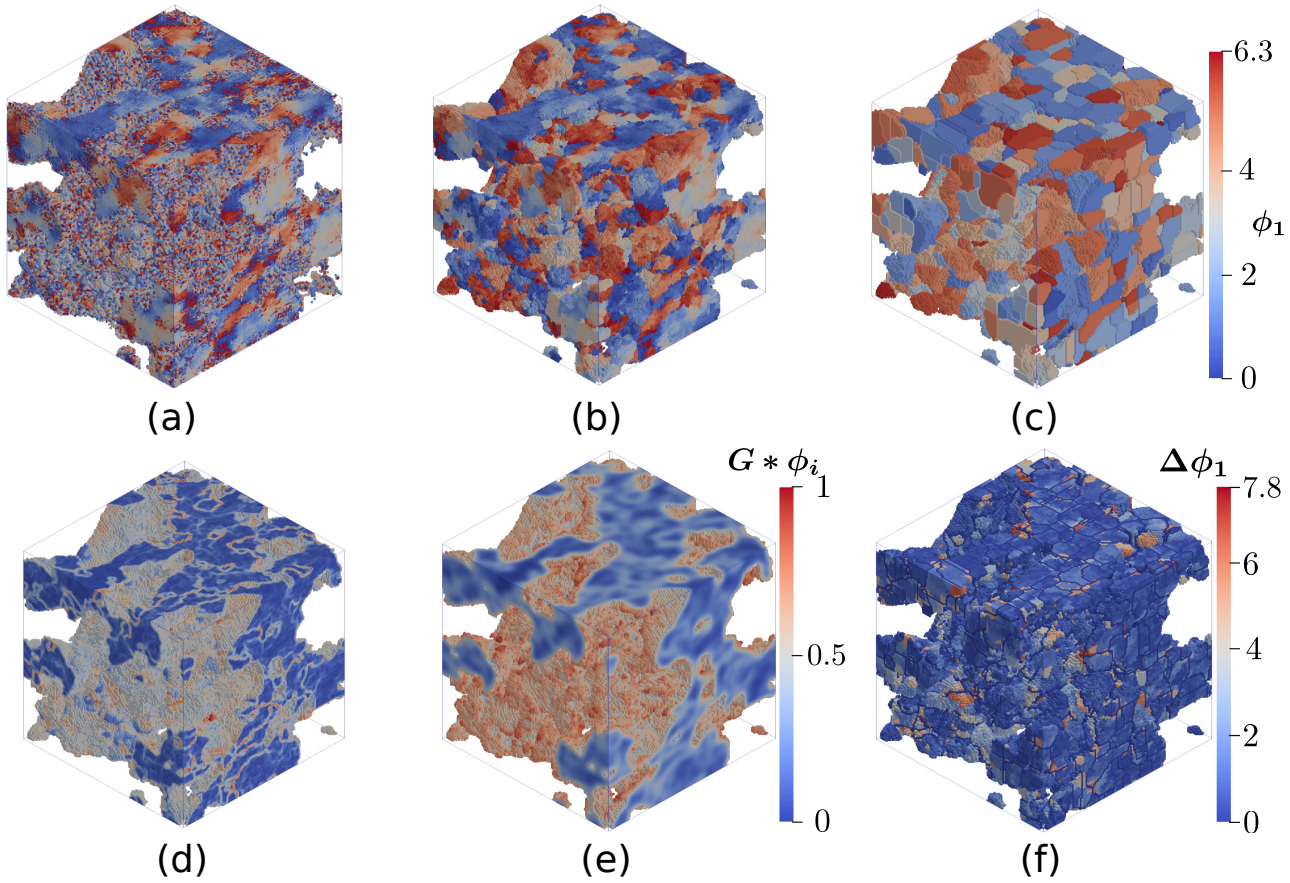


Supplementary Figure 1: Experimental setup and tensile data for the AA7050 alloy. (a) Dogbone samples showing the deposition paths of cold spray forming, (b) True stress-true strain (σ-ϵ) response from mechanical tension test along the X and Y directions. The range corresponds to the minimum and maximum values of the true stress observed in the experiments.

II. Additional details on generating SEVMs for CSF Al7050

i. Post-processing steps using SliceGAN

Grains in the microstructure are difficult to distinguish from the direct SliceGAN output. Supplementary Figure 2(a), showing the Euler angle component ϕ_1 from the SliceGAN results, exhibits considerable noise. Two post-processing steps are necessary to obtain a distinct demarcation of grains. These include a minimum grain size thresholding as shown in Supplementary Figure 2(b), and a watershed filter shown in Supplementary Figure 2(c). The watershed filter uses the gradients of the Euler angles, which are computed using Sobel operators. Supplementary Figure 2(d) shows the sum of the gradients of each Euler angle component $SGE = \sum_{i=1}^{3} G\phi_i$, where G is the magnitude of the gradient computed as $G = \sqrt{G_x + G_y + G_z}$. Here $G_x = S_x * \phi_i$, $G_y = S_y * \phi_i$, and $G_z = S_z * \phi_i$ are the derivatives in the three orthogonal directions. S_x, S_y, and S_z are the kernels weighting functions in the Sobel operator, ϕ_i are the components of the Euler angles,

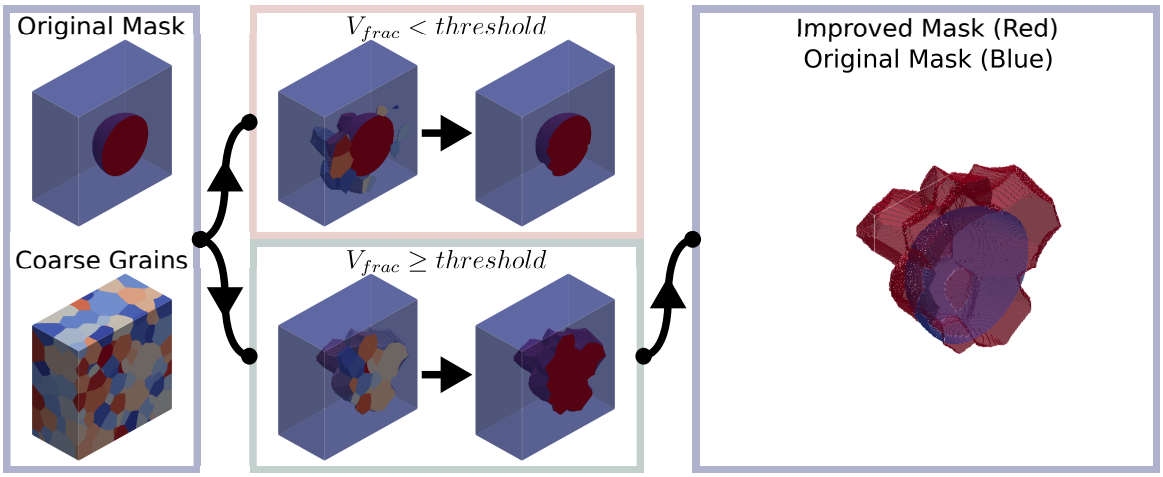


Supplementary Figure 2: Post-processing steps for Euler angles obtained using the SliceGAN code. (a) Euler angle component ϕ_1 directly obtained from SliceGAN, (b) voxel size and gradient denoising, (c) average Euler angle from step (b) within each watershed basin, (d) sum of gradients of each Euler angle component, (e) gradients from step (d) after contrast and Gaussian blur, and (f) difference between denoised Euler angles from step (b) and watershed basin average Euler angles from step (c).

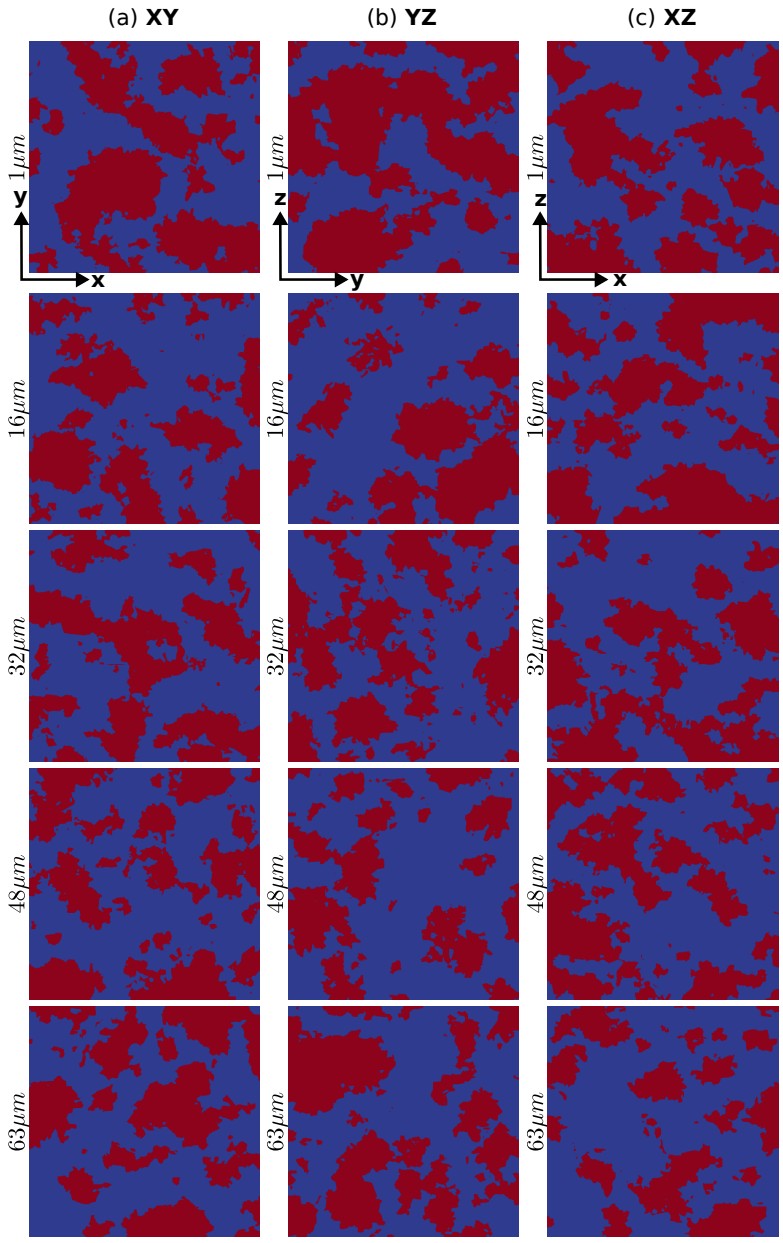
and $*$ is a convolutional operator. SGE values close to 1 correspond to grain boundaries. The gradient field is processed using a contrast filter and a Gaussian blur filter, as shown in Supplementary Figure 2(e). The difference between the denoised SliceGAN output and the average Euler angle within each watershed basin is shown in Supplementary Figure 2(f).

ii. Post-processing steps using the SliceGAN-DREAM.3D platform

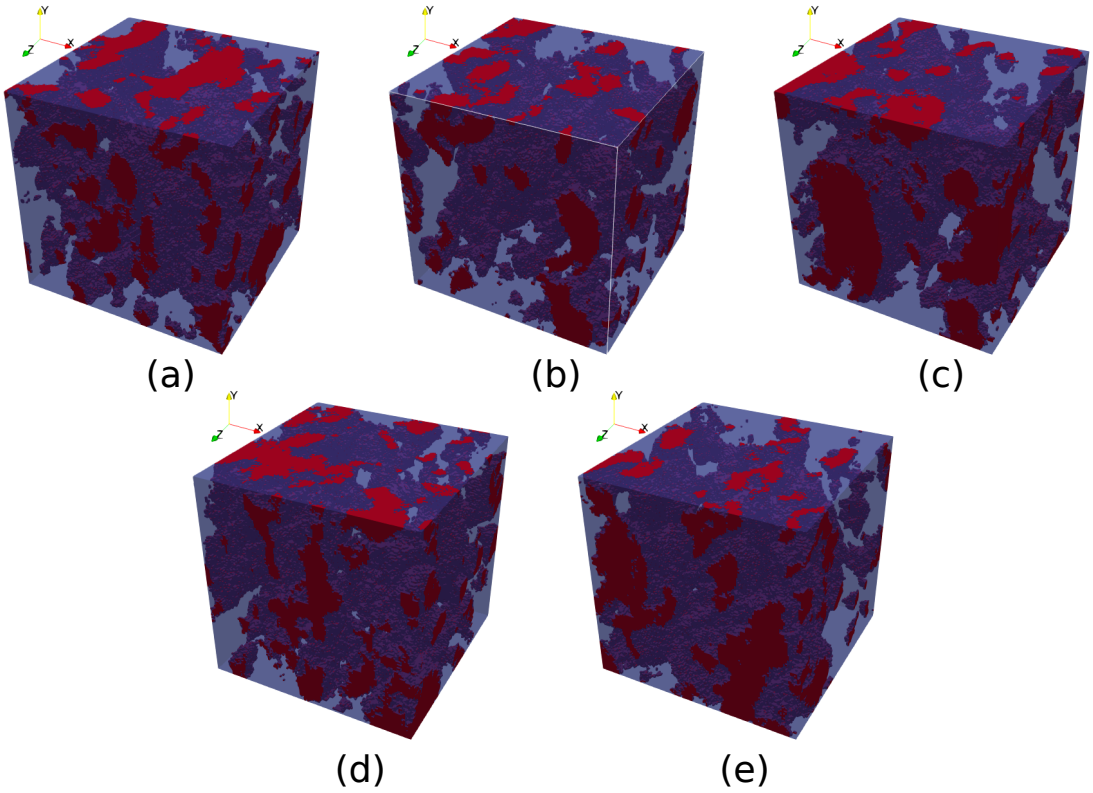
The schematic in Supplementary Figure 3 shows the process of creation of an improved mask similar to that seen in Figure 9(f). The original mask generated by SliceGAN (approximated as a sphere just for the schematic representation), is used as an initial guide to create the actual region containing the coarse grains. All coarse grains, matching the criteria given in Equation (6) are retained, and hence the original mask is expanded to contain all voxels belonging to those grains. All grains not matching the criteria in Equation (6) are eliminated, such that the original mask is dilated to remove all voxels belonging to those grains. Using a volume fraction $V_{frac} = 0.5$ should result in a mask that is similar in volume fraction to the original, whereas a $V_{frac} < 0.5$ should result in a mask with a higher volume fraction.



Supplementary Figure 3: Visual representation showing steps in the creation of an improved mask similar to that seen in Figure 9(f).



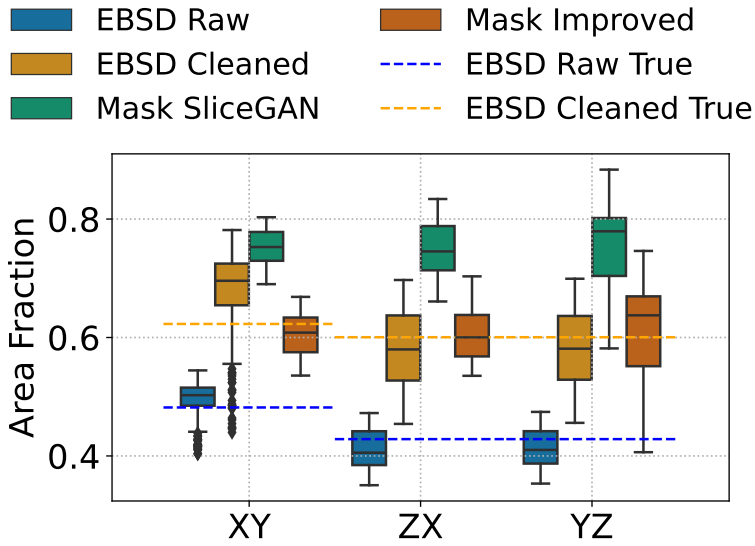
Supplementary Figure 4: Slices of the 3D binary microstructure constructed with SliceGAN. (a) XY, (b) YZ and (c) XZ planes at 1 µm, 16 µm, 32 µm, 48 µm and 63 µm from the surface.



Supplementary Figure 5: Different bimodal microstructures generated using SliceGAN alone. The microstructures have similar characteristics to the binary microstructure obtained in step 2 (Generating binary 3D SEVMs) directly from SliceGAN.

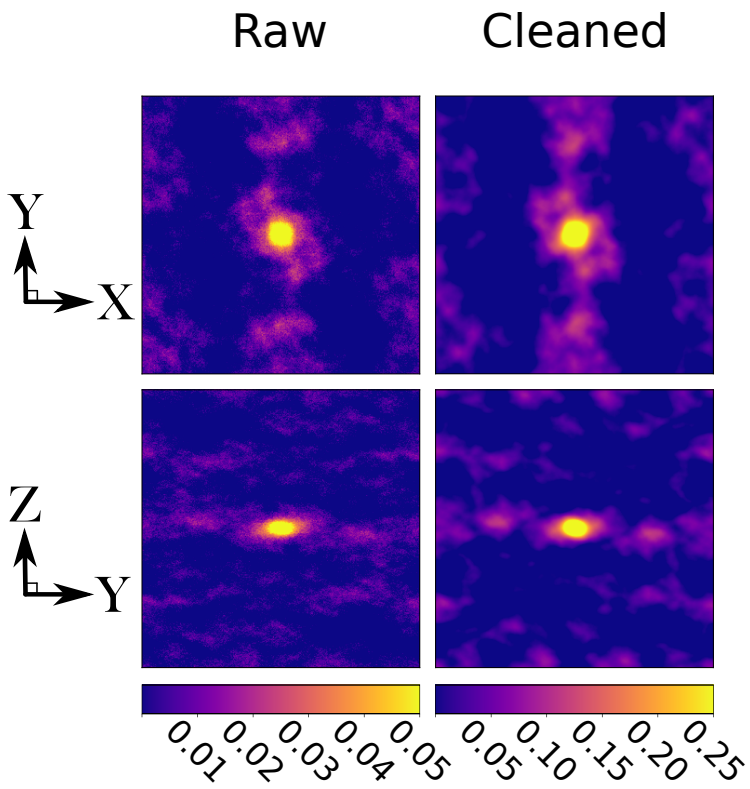
Supplementary Figure 6 shows box plot expressions of much of the same data contained in the PDF plots of Figure 9(g) with a few key additions. To see the effect of the grain cluster thresholding on the distributions, it includes the area fractions of the EBSD data after thresholding out the UFGs, but before thresholding out the small pockets of CG clusters for SliceGAN training. It is observed that the grain cluster thresholding operation primarily stretches and shifts the distributions upwards. Additionally, the figure shows dashed lines denoting the singular area fractions of the full EBSD maps. Because SliceGAN requires sub-sampling rectangular windows of the EBSD images for training, there exists a sampling bias such that there is a decreasing gradient from the center to the edges of the EBSD images of the probability of data being included in a given sample. This sampling bias can be seen clearly in the deviation from the mean of the EBSD-Cleaned distribution versus the EBSD-Cleaned True value in the XY plane. While the true value is the most important to match the results, it is also important to understand the bias that went into training the GAN. It can also be seen clearly

in Supplementary Figure 6 that the mask improvement process does not affect the shape of the area fraction distributions in a major way, but instead shifts the distributions downwards. It can be seen here that the shift has the effect of closely aligning the mean of the SEVM mask area fraction distributions with the true area fractions of the cleaned EBSD data.

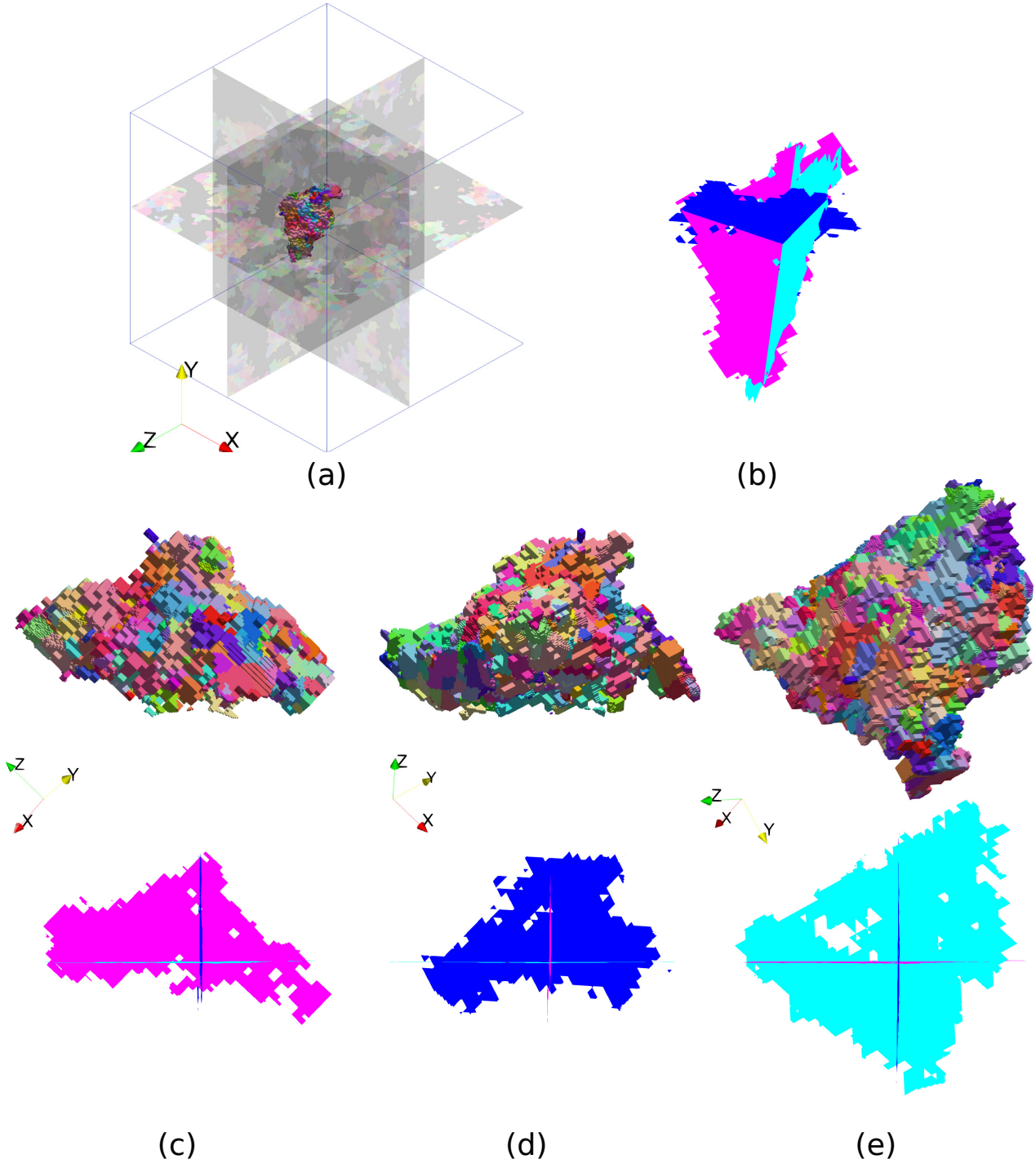


Supplementary Figure 6: Box and whisker plots comparing the area fractions ($\frac{A_{UFG}}{A_{Total}}$) of 300 $64\,\mu m$ $\times$ $64\,\mu m$ samples of the 2D experimental (EBSD) data after GAKAM thresholding (EBSD Raw) and after grain cluster thresholding (EBSD Cleaned), and of the 3D binary mask used to create the SEVM directly from SliceGAN (Mask SliceGAN) and after the mask improvement operation (Mask Improved). EBSD Raw True and EBSD Cleaned True are the area fractions of their respective EBSD data without sub-sampling.

A comparison of the 2-point correlation S_2 of the prior particle phase before and after performing the thresholding and erode/dilation is depicted in Supplementary Figures 7 for the EBSD (Raw data) and EBSD (Cleaned data) in the XY and XZ planes. From these results, it can be inferred that the morphology of the prior particle domain is not altered significantly as the general shape of the S_2 function remains almost unchanged. This can also be seen in Figures 9(b, c), where the prior particle shape did not change.



Supplementary Figure 7: Comparison of the 2-point correlation function S_2 maps of the EBSD data just after the GAKAM threshold to isolate coarse grains as shown in Figure 2 (Raw), and just after the grain cluster size threshold as shown in Figure 9(c,d) (Cleaned).



Supplementary Figure 8: Particle morphology details. (a) Details of a prior particle picked from the center of the 3D SEVM created using the integrated SliceGAN-DREAM.3D platform. (b) Three orthogonal planes along the particle are colored magenta, blue, and cyan. View of the particle perpendicular to the (c) magenta, (d) blue, and (e) cyan planes to provide a clear view of the prior particle geometry.

III. Micromechanical crystal plasticity and upscaled constitutive models

Micromechanical analysis of the CGs in the concurrent SEVM models is conducted with a crystal plasticity finite element model (CPFE) [8]. The stress-strain constitutive equation is expressed in a thermally-expanded intermediate configuration as:

$$\boldsymbol{S} = \mathbb{C} : \boldsymbol{E_e} \tag{S1}$$

where $\boldsymbol{S}$ is the 2nd Piola-Kirchhoff stress tensor, $\mathbb{C}$ is the temperature dependent anisotropic elasticity tensor, and $\boldsymbol{E_e}$ is the elastic Green-Lagrange strain tensor. The elastic Green-Lagrange strain tensor is related to the elastic deformation gradient, obtained from the multiplicative decomposition of the deformation gradient $\boldsymbol{F}$ into plastic $\boldsymbol{F_p}$, thermal $\boldsymbol{F_\theta}$ and elastic $\boldsymbol{F_e}$ components ($\boldsymbol{F} = \boldsymbol{F_e F_\theta F_p}$) as:

$$\boldsymbol{E_e} = \frac{1}{2}(\boldsymbol{F_e}^{\boldsymbol{T}}\boldsymbol{F_e} - \boldsymbol{I}) \tag{S2}$$

where $det\boldsymbol{F_p} = 1$ and $\dot{\boldsymbol{F}}_{\boldsymbol{\theta}} = \dot{\theta}\boldsymbol{\alpha F_\theta}$. The plastic velocity gradient $\boldsymbol{L_p}$ is related to the slip rate $\dot{\gamma}^\alpha$ as:

$$\boldsymbol{L_p} = \dot{\boldsymbol{F}}_{\boldsymbol{p}}\boldsymbol{F_p}^{-\mathbf{1}} = \sum_{\alpha}^{n_s} \dot{\gamma}^\alpha \boldsymbol{s}_0^\alpha, \tag{S3}$$

where n_s, α, and $\boldsymbol{s}_0^\alpha = \boldsymbol{m}_0^\alpha \bigotimes \boldsymbol{n}_0^\alpha$, are respectively the number of slip systems, slip system, and the Schmid tensor defined in terms of the slip direction $\boldsymbol{m}_0^\alpha$ and the slip plane $\boldsymbol{n}_0^\alpha$. A thermally activated flow rule is used to represent the slip rate $\dot{\gamma}^\alpha$ in terms of the driving stress σ^α as:

$$\dot{\gamma}^\alpha = \dot{\gamma}^\alpha_{ref} exp\left(\frac{Q^\alpha_{slip}}{K_B\theta}\left[1 - \left(\frac{|\sigma^\alpha| - s^\alpha_a}{s^\alpha_\star}\right)^P\right]^Q\right), \text{ with } \sigma^\alpha = \tau^\alpha - \chi^\alpha, \tag{S4}$$

where $\dot{\gamma}^\alpha_{ref}$ is the reference slip rate, Q^α_{slip} is the thermal activation energy, K_B is the Boltzmann constant, θ is the temperature, and P and Q are materials constants. The driving stress is obtained from the resolved shear stress τ^α and the back stress χ^α. The athermal and thermal slip resistances, s^α_a and $s^\alpha_\star$, consider both statistically stored dislocations (SSDs) and geometrically necessary dislocations (GNDs) as:

$$s^\alpha_a = s^\alpha_{a,0} + \sqrt{(s^\alpha_{a,SSD})^2 + (s^\alpha_{a,GND})^2} \text{ and } s^\alpha_\star = s^\alpha_{\star,0} + \sqrt{(s^\alpha_{\star,SSD})^2 + (s^\alpha_{\star,GND})^2}, \tag{S5}$$

where $s^{\alpha}_{a,0}$ and $s^{\alpha}_{\star,0}$ are the initial resistances and the evolution of the thermal and athermal SSDs is defined using a phenomenological hardening equation as:

$$\dot{s}^{\alpha}_{a,SSD} = \sum_{\beta=1}^{n_s} h^{\alpha\beta}_{a} |\dot{\gamma}^{\beta} sin(\boldsymbol{n}^{\alpha}_{0}, \boldsymbol{t}^{\beta}_{0})| \text{ and } \dot{s}^{\alpha}_{\star,SSD} = \sum_{\beta=1}^{n_s} h^{\alpha\beta}_{\star} |\dot{\gamma}^{\beta} cos(\boldsymbol{n}^{\alpha}_{0}, \boldsymbol{t}^{\beta}_{0})|, \tag{S6}$$

where $\boldsymbol{t}_0$ is the direction of the dislocation line, $h^{\alpha\beta}$ is the hardening of slip system α due to the activity on slip system β. The shear resistances related to the GNDs are given as:

$$s^{\alpha}_{a,GND} = c_1 G b \sqrt{\rho^{\alpha}_{P,GND}} \text{ and } s^{\alpha}_{a,GND} = \frac{Q^{\alpha}_{slip}}{c_2 c_3 b^2} \sqrt{\rho^{\alpha}_{F,GND}}, \tag{S7}$$

where G is the shear modulus, c_1, c_2 and c_3 are material constants, b the Burger's vector, and Q^{α}_{slip} the activation energy. $\rho^{\alpha}_{P,GND}$ and $\rho^{\alpha}_{F,GND}$ are the pararel and forest GND density and are calculated using the curl of the plastic deformation gradient or Nye's Tensor $\boldsymbol{\Lambda} = \nabla \times \boldsymbol{F_p}$.

The upscaled constitutive model (UCM), following steps in [61, 62], is used to model UFGs in the concurrent SEVM model. The UCM is based on a constitutive model that is thermodynamically consistent with the homogenized behavior of the underlying SERVE response in crystal plasticity-based micromechanical simulations. Detailed concepts of the development of UCMs are given in [61, 62]. The plastic velocity gradient $\boldsymbol{L_p}$ is approximated to its symmetric part, the plastic rate of deformation $\boldsymbol{D_p}$, and is expressed by the power law as:

$$\boldsymbol{L_p} \approx \boldsymbol{D_p} = \dot{\boldsymbol{F}}_{\boldsymbol{p}} \boldsymbol{F}_{\boldsymbol{p}}^{-1} = D_0 \left(\frac{Y}{Y_0} \right)^{\frac{1}{m}} \boldsymbol{N} \tag{S8}$$

where D_0 is a reference strain rate and m is the rate sensitivity parameter. An anisotropic plastic yield function with tension-compression asymmetry is assumed as:

$$Y = [(|\lambda_1| - k\lambda_1)^a + (|\lambda_2| - k\lambda_2)^a + (|\lambda_3| - k\lambda_3)^a]^{1/a} \tag{S9}$$

where a and k are the exponent that determines the smoothness of the yield surface and tension-compression asymmetry parameter, respectively. λ_1, λ_2 and λ_3 are the eigenvalues of a transformed second Piola-Kirchhoff stress tensor given as:

$$\boldsymbol{\Sigma} = \mathbb{L} : (\boldsymbol{S} - \boldsymbol{\chi}), \tag{S10}$$

where $\mathbb{L}$ is a fourth-order transformation matrix that can introduce anisotropy to the yield function with a tensor defined by 21 independent coefficients. For orthotropy, the transformation matrix is defined by six independent

variables as:

$$\mathbb{L} = \begin{bmatrix} \alpha_1 & \beta_1 & \beta_2 & 0 & 0 & 0 \\ \beta_1 & \alpha_2 & \beta_3 & 0 & 0 & 0 \\ \beta_2 & \beta_3 & \alpha_3 & 0 & 0 & 0 \\ 0 & 0 & 0 & \gamma_1 & 0 & 0 \\ 0 & 0 & 0 & 0 & \gamma_2 & 0 \\ 0 & 0 & 0 & 0 & 0 & \gamma_3 \end{bmatrix}, \tag{S11}$$

By using the isochoric plastic flow condition $\beta_1 = 0.5(\alpha_3 - \alpha_2 - \alpha_1)$, $\beta_2 = 0.5(\alpha_2 - \alpha_3 - \alpha_1)$ and $\beta_3 = 0.5(\alpha_1 - \alpha_2 - \alpha_3)$. In the present work, the deformation of the UFGs is defined by an isotropic transformation matrix, i.e., $\alpha_1 = \alpha_2 = \alpha_3 = \dfrac{2}{3}$ and $\gamma_1 = \gamma_2 = \gamma_3 = 1$.

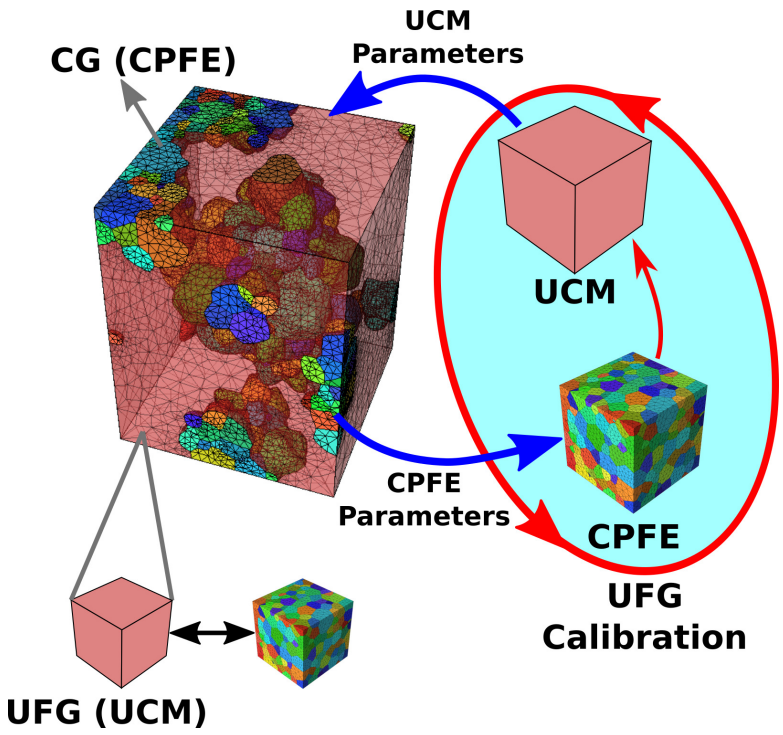
The evolution of the yield resistance is represented by a modified Voce-type law given as:

$$Y_0 = Y_{ref} + Y_{sat} exp\left(-\left(\frac{\varepsilon_p}{\beta}\right)^{\psi}\right) + \alpha(1 - exp(-b\varepsilon_p)) \tag{S12}$$

where Y_{ref} is the initial yield resistance, $\psi = 0.75$, $b = 0.5$, and Y_{sat}, β, and α are material parameters. The effective plastic strain is defined using the deviatoric part of the plastic rate of deformation $\boldsymbol{D_p^{dev}}$ as:

$$\varepsilon_p = \int_0^t \sqrt{\frac{2}{3}\boldsymbol{D_p^{dev}} : \boldsymbol{D_p^{dev}}}\, dt \tag{S13}$$

The calibration procedure is illustrated in Supplementary Figure 9. It is comprised of two loops, viz. (i) an outer loop that compares the mechanical response of the complete bimodal SEVM to the experimental data and (ii) an inner loop where the stress-strain response by the UCM matches the stress-strain response by the crystal plasticity model for the UFGs.

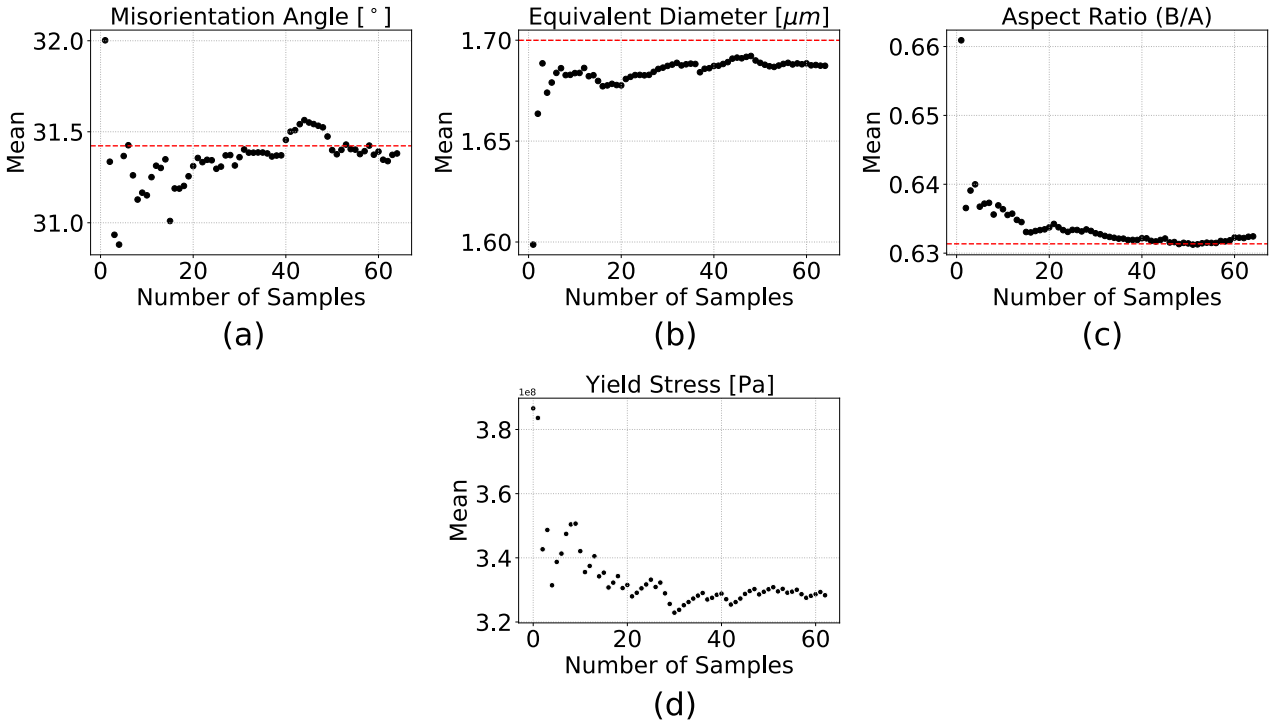


Supplementary Figure 9: Sequence of steps for calibrating material parameters in the bimodal SEVM model. The mechanical behavior of the CGs is modeled using a crystal plasticity (CP) model while modeling the UFGs uses an upscaled constitutive model (UCM). The calibration has an outer loop in red and an inner loop in blue. The outer loop compares the stress-strain behavior of the bimodal SEVM and the experimental data, while the inner loop compares the UFG behavior using CPFE and UCM-based FE simulations.

IV. FE simulation strategy of the SEVMs for mechanical response

The large size of the SEVM containing a high number of CGs makes direct FE analysis using CPFEM, computationally prohibitive. To overcome this limitation, the SEVM can be divided into smaller sub-volume elements (SVEs) for performing FE analysis. The overall mechanical response of each SVE can be averaged over a large number of SVEs to obtain the overall SEVM response. For the viability of such analysis in terms of overall accuracy and reduced computational time, it is important to determine the number of SVEs that should be considered.

Two convergence tests are performed to estimate this number. In the first set of tests, the microstructure-based SVEs (M-SVE) are based on the convergence of morphological and crystallographic characteristics of the microstructure. Supplementary Figures 10(a-c) plot the mean grain size, grain aspect ratio, and misorientation angle as a function of the number of M-SVEs sampled. During sampling of the SVEs from the SEVM, their boundaries can intersect a large number of grains. A special technique, which averages SVE statistics with and without intersected grains is implemented for these plots. The red dashed line corresponds to the average value of the microstructural descriptor function for the entire SEVM generated by the integrated SliceGAN-DREAM.3D platform. Convergence with respect to the red line, within an assumed tolerance, estimates the minimum number of M-SVEs required for micromechanical analysis for property assessment. The equivalent diameter converges with approximately 10 M-SVEs corresponding to a maximum error of 5.8% in Supplementary Figure 10(a). The aspect ratio converges with a maximum error of 4.5% for approximately 30 SVEs in Supplementary Figure 10(b). In Supplementary Figure 10(c), the misorientation angle reaches convergence with a maximum error of 1.9% in approximately 20 SVEs. The oscillatory behavior of the misorientation angle convergence is a consequence of the two peaks on the misorientation angle distribution.

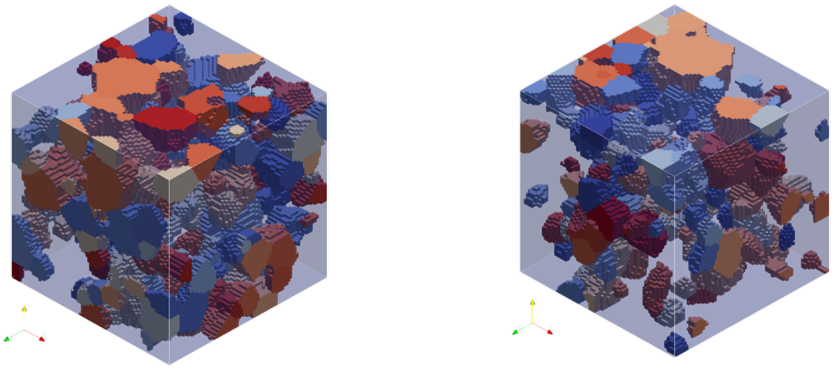


Supplementary Figure 10: Convergence plots of microstructural descriptors and properties for estimating microstructure and property-based statistical volume elements (M-SVE and P-SVE) taken from the SEVM. M-SVE convergence with respect to (a) misorientation angle, (b) equivalent diameter, (c) aspect ratio, and (d) P-SVE convergence with respect to yield stress. The red dashed lines show the average value of the given microstructural characteristic/property for all grains in the SEVM, and the blue points correspond to the averaged property value over N SVEs.

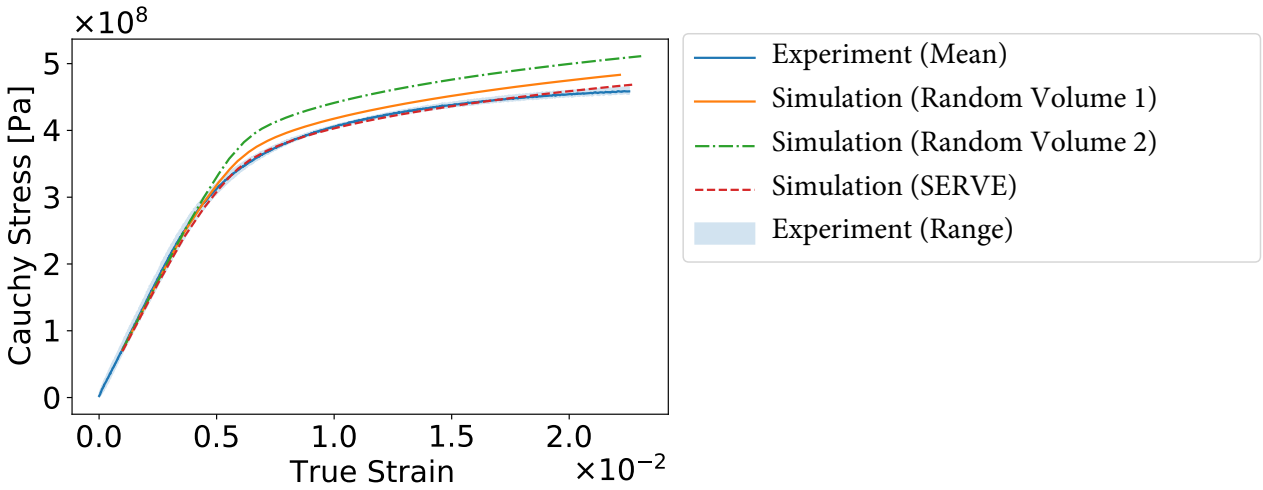
The second test corresponds to the convergence of property-based SVE (P-SVE) with respect to a chosen property or response function. The property is determined from micro-mechanical analysis of the SVEs. Each SVE contains both CGs and UFGs in their domain that are modeled by two different constitutive models. In Supplementary Figure 10(d) the convergence in the SVE yield stress is shown through a plot as a function of the number of P-SVEs sampled. The plot has an oscillatory behavior for a lower number of samples but reaches convergence for approximately 40 samples. The M-SVE and P-SVE convergence analysis shows that approximately 40 SVE samples are necessary to capture the properties of the SEVM presented in Supplementary Figure 10(d). This number of samples also ensures that the complexity in the geometry of the microstructure is statistically well-represented.

Comparing the macroscopic response of the created SERVE with other randomly generated microstructures

To show the need for accurate mask geometry and distributions in the material simulation, as opposed to a randomly created microstructure, results of additional tests are performed and shown in Supplementary Figure 11(b). The random microstructure 1 has the same UFG volume fraction of 0.6 as the SERVE, while the random microstructure 2 has a UFG volume fraction of 0.75. Random aspect ratio and misorientation distributions, viz. the Mackenzie distribution, are assigned to the volumes as shown in Supplementary Figure 11(a). For the random volumes 1 and 2, the mask is generated by selecting grains randomly and assigning CP and UFG properties. The overall stress-strain response of the three different simulated microstructures (Simulation: (SERVE), (Random Volume 1), and (Random Volume 2)) are compared with the experimental data in Supplementary Figure 11(b). It is observed that the randomness of the mask can significantly change the response of the material and hence a more rigorous method such as that in this paper is desirable.



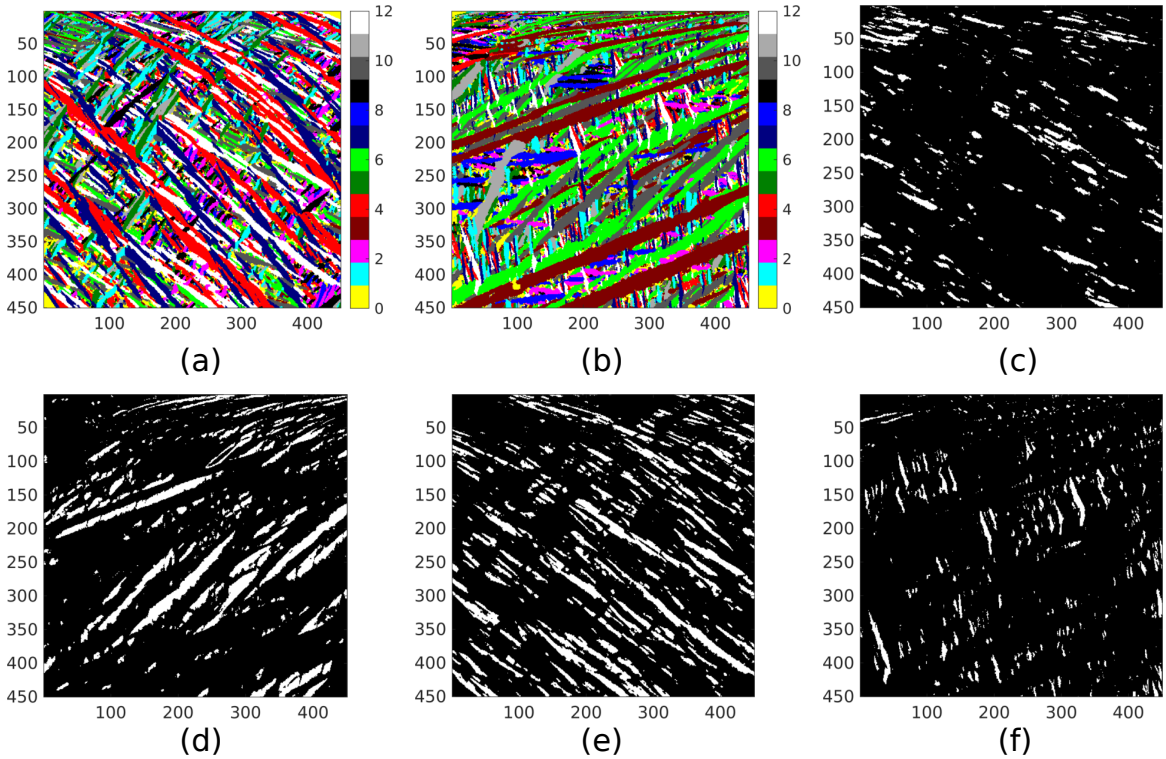
(a)



(b)

Supplementary Figure 11: (a) Microstructures Random volume 1 with a UFG volume fraction of 0.6 and Random volume 2 with a UFG volume fraction of 0.75 with randomly assigned aspect ratio and misorientation angle distribution, and (b) comparison of the stress-strain plots for the different microstructural volumes with experimental results.

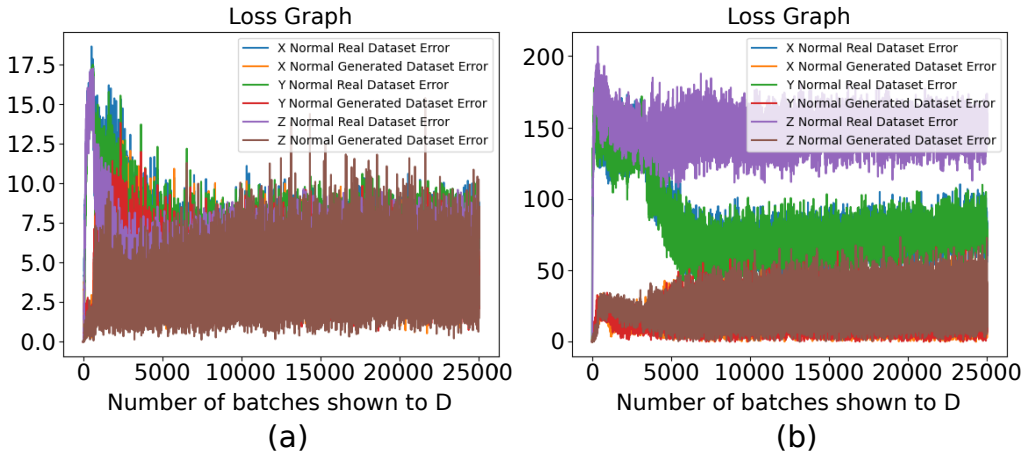
V. Characteristics of experimentally acquired EBSD images of additively manufactured Ti64 alloy



Supplementary Figure 12: Input details for the creation of the Ti64 microstructure. Variants of the Ti64 microstructure in the plane (a) XY and (b) YZ. Binary microstructure of variant 10 in the plane (c) XY and (d) YZ. Binary microstructure of variant 12 in the plane (e) XY and (f) YZ.

VI. Loss curves during training for the creation of the CS Al microstructure and the additively manufactured Ti64 alloy

Supplementary Figure 13 shows the discriminator loss evolution during training, calculated using Equation (4). The loss evolution approaches a constant value. The number of batches shown to the discriminator is selected such that the evolution of the loss is stable. The number of batches is also chosen to avoid mode collapse and an abrupt increase in the loss function. The evolution of the loss function can be improved by using more data or other changes in the model as explained in the Discussion section.



Supplementary Figure 13: Loss function plots for training the GAN model to create: (a) the cold spray formed AA7050 microstructure and (b) the additively manufactured Ti64 alloy microstructure.